Nanoscale

Accepted Manuscript

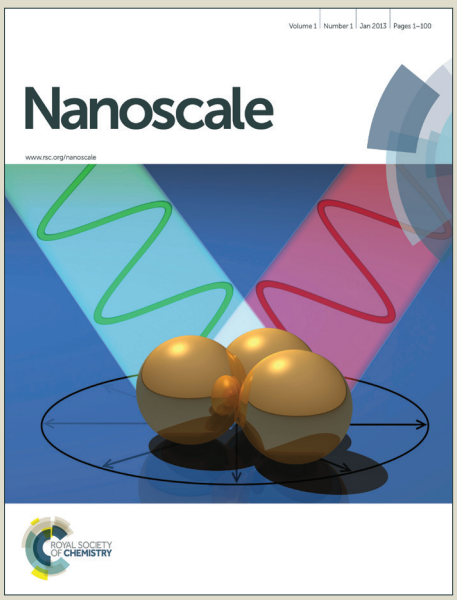

ROYAL SOCIETY OF CHEMISTRY

www.rsc.org/nanoscale

Cite this: DOI: 10.1039/c0xx00000x

www.rsc.org/xxxxxx

ARTICLE TYPE

Improved Electrochemical Performance of Nitrogen Doped TiO_2-B Nanowires as Anode Material for Li-ion Batteries

Yongquan Zhang,[a] Qiang Fu,[a] Qiaoling Xu,[a] Xiao Yan,[b] Rongyu Zhang,[a] Zhendong Guo,[a] Fei Du,[a] Yingjin Wei,*[a] Dong Zhang,[a] and Gang Chen[a, c]

Received (in XXX, XXX) XthXXXXXXXXX 20XX, Accepted Xth XXXXXXXXX 20XX
DOI: 10.1039/b000000x

N-doped TiO_2-B nanowires are prepared by the solvothermal method using TiN nano particles as the starting material. X-ray photoelectron spectroscopy shows that the N dopants preferentially occupy the interstitial sites of TiO_2-B up to a content of ~ 0.55 at.%. Above this critical value, the N dopants will substitute the oxygen atoms which improve the electronic conductivity of TiO_2-B. The maximum proportion of substituted-N in the TiO_2-B nanowires is ~ 1.3 at.%. Raman scattering shows that the substituted-N strengthens the Ti(1)-O_1-Ti(2) and O_1-Ti(1)-O_3 bonds of TiO_2-B. This improves the stability of the corresponding local structures thus depressing the distortion of the Li^+ diffusion channel along the *b*-axis of TiO_2-B. As a result, the substituted-N plays more effective impacts on the electrochemical properties of TiO_2-B than the interstitial-N does. The TiO_2-B nanowires containing substituted-N dopants exhibit remarkably enhanced electrochemical performance than that of pure TiO_2-B. It shows a discharge capacity of 153 mAh g^{-1} at the 20 C rate with capacity retention of 76 % after 1000 cycles. In addition, it can deliver a discharge capacity of 100 mAh g^{-1} at an ultra-high rate of 100 C, indicating its great potential in high power lithium ion batteries.

1. Introduction

Lithium ion batteries have been considered as one of the most prominent energy storage devices due to their high energy densities and long cycle life. Conventional lithium ion batteries use graphite as the anode material which is cheap, abundant and stable for cycling. However, both natural graphite and artificial graphite have severe safety concerns because they operate close to the Li^+/Li redox couple with a risk of metallic lithium plating and dendrite formation at overcharged state.[1] In addition, they suffer from a high irreversible capacity loss during initial cycles due to the formation of a solid electrolyte interphase (SEI) film.[2] As a consequence, searching for alternative anode materials is strongly required for the development of next generation of lithium ion batteries.

In various new anode materials under consideration, titanium dioxides (TiO_2) including anatase, rutile and bronze (TiO_2-B) have attracted particular attention because of their long cycle life, high safety and minimum environmental impact.[3-10] The higher redox potential of titanium dioxides (~ 1.6 V vs. Li/Li^+) endows them with greater overcharge protection than graphite. In addition, the material can be easily made in nanostructured forms thus permitting access to fast charge-discharge rates. A major problem for the TiO_2 anodes is their high working voltages compromising the cell voltage and hence the energy density. This shortcoming can be partly overcome by coupling with high voltage cathode materials such as $LiNi_{0.5}Mn_{1.5}O_4$ (4.7 V vs. Li/Li^+), or high capacity cathode materials such as Li-excess layered oxides $Li[Li_xM_{1-x}]O_2$ (M = Mn, Ni, Co).[11-13]

Among different titanium dioxides, TiO_2-B is the most attractive one due to its large specific capacity and excellent rate capability. TiO_2-B can store more than 250 mAh g^{-1} in its nanostructured forms.[14-16] In contrast, the practical specific capacities of anatase and rutile TiO_2 are limited to 168 mAh g^{-1}. However, the electrochemical performance of TiO_2-B is seriously restricted by its low electronic conductivity and small lithium diffusion coefficients. These problems can be overcome by preparing nano structured TiO_2-B combining with carbonaceous additives such as carbon nanotubes, carbon fibers, and graphene etc.[17-22] But, the carbonaceous additives can only tailor the electron transport on the particle surface and between adjacent particles; the intrinsic electronic conductivity of the TiO_2-B bulk is still poor. In addition, the carbonaceous additives in the composite anodes decrease the tap density of the materials thus sacrifice the energy density of the battery.

[a]*Key Laboratory of Physics and Technology for Advanced Batteries (Ministry of Education), College of Physics, Jilin University, Changchun 130012, P. R. China.*
[b]*CAS Key Laboratory of Biobased Materials, Qingdao Institute of Bioenergy and Bioprocess Technology, Chinese Academy of Sciences, Qingdao, 266101, P. R. China.*
[c]*State Key Laboratory of Superhard Materials, Jilin University, Changchun 130012, P. R. China.*
Corresponding author: yjwei@jlu.edu.cn (Y. J. Wei)
Tel & Fax: 86-431-85155126
† Electronic Supplementary Information (ESI) available. See DOI: 10.1039/b000000x/

Recently, it has shown that the intrinsic electronic conductivity of TiO_2 can be improved by doping of some aliovalent ions such as Nb^{5+}, V^{5+}, P^{5+}, Fe^{3+}, Zn^{2+}, N^{3-}, S^{2-} and F^-.[23-31] In addition, slight modification of the TiO_2 lattice can be achieved by the dopant atoms which may improve the diffusion of lithium ions. For example, J. G. Kim et al. prepared N-doped TiO_2 nanofibers by the electrospining method. The N-doped nanofibers showed a discharge capacity of 185 mAh g^{-1} at the 0.1 C rate, which was much higher than that of the un-doped counterpart.[32] H. K. Han et al, reported that the discharge capacity of N-doped TiO_2 hollow nanofibers (85 mAh g^{-1}) at the 2 C rate was nearly two times higher than that of ordinary TiO_2 nanoparticles.[29] G. Liu et al. prepared N and S co-doped TiO_2 nanocrystals. The material showed superior rate performance due to its high electronic conductivity.[30] Y. M. Li et al. reported that the N-doped anatase TiO_2 and N-doped graphene nanocomposite showed much better electrochemical performance than that of pristine TiO_2.[33] In addition, our recent work showed that the lithium diffusion coefficients of N-doped anatase TiO_2 were increased about 13 times with respect to its un-doped counterpart.[34] These works suggest that N doping could be a proper method for improving the electrochemical properties of TiO_2-B. However, to the best our knowledge, there is no work to study the effects of N-doping on the electrochemical properties of TiO_2-B. In this work, for the first time, we prepared N-doped TiO_2-B nanowires by the solvothermal method. The material shows good cycle stability and excellent rate capability for Li ion storage which indicates its potential applications in high power lithium ion batteries. In order to reveal the origins for the excellent electrochemical performance, the physical and structural properties of the materials were studied by X-ray photoelectron spectroscopy and Raman scattering, Their electrochemical kinetic properties were studied by cyclic voltammetry, electrochemical impedance spectroscopy and galvanostatic intermittent titration technique.

2. Experimental section

2.1 Synthesis of N-doped TiO_2-B nanowires

The N-doped TiO_2-B nanowires were prepared by using commercial TiN nano particles (T110281, Aladdin) as the starting material. The TiN nano particles were heat treated at 400 ^oC in air to obtain the N-doped TiO_2 precursors. The contents of N in the precursors were adjusted by changing the heat treatment time from zero minute to 30 minute. To prepare pure TiO_2-B nanowires, the heat treatment temperature was increased to 500 ^oC and the heating time was elongated to 10 h. The pure and N-doped TiO_2-B nanowires were synthesized by the hydrothermal reaction of the above precursors. As a typical procedure: 0.4 g of the precursor powders were dispersed in 40 mL of 10 mol L^{-1} NaOH solution. The suspension was transferred into a 50 ml autoclave. The autoclave was then sealed and heat treated at 170 ^oC for 60 h. After cooling to room temperature, the obtained precipitates were isolated from the solution, followed by constant stirring in 0.1 mol L^{-1} of HCl solution for 4 h to obtain proton exchanged titanate precipitate. The precipitate was then centrifuged and washed completely with deionized water. Afterwards, the material was freeze-dried at -30 ^oC for 20 h. Finally, the material was heat treated at 450 ^oC for 4 h in N_2 flow to improve the crystallization of the products.

2.2 Materials characterizations

The crystal structure of the materials was studied by X-ray diffraction (XRD) on a Bruker AXS D8 X-ray diffractometer with Cu Kα radiation. The lattice parameters were calculated by the Celref 3 Program. The morphology of the materials was studied by JSM-6700F field emission scanning electron microscope (FESEM). High-resolution transmission electron microscope (HRTEM) was taken on a FEI Tacnai G2 electron microscope coupled with an X-ray energy dispersive spectroscopy (EDS, BRUKER AXS). Raman scattering of the products was collected on a Thermo Scientific FT-Raman using Nd-line laser source (λ = 532 nm). X-ray photoelectron spectroscopy (XPS) was performed on an ESCALAB spectrometer using Mg-Kα light source. The binding energy was corrected using the C 1s peak at 284.6 eV. For measurement of electronic conductivity, the samples were prepared to thin film electrodes on a copper substrate with thickness about 30 μm. Then, *dc* conductivity measurement was performed by the two-electrode method.

Electrochemical experiments were performed using 2032 coin cells with metallic lithium foil as the anode. The cathode was composed of 70 wt.% active material, 15 wt.% super P conductive additive and 15 wt.% poly-vinylidenefluoride (PVDF) binder which was pasted on a copper current collector. The loading mass of active material was 1~2 mg cm^{-2}. The anode and cathode were separated by Celgard 2320 membrane. A 1 mol L^{-1} lithium hexafluorophosphate ($LiPF_6$) dissolved in ethylene carbonate (EC) and dimethyl carbonate (DMC) (EC: DMC = 3: 7) was used as the electrolyte. Galvonostatic charge-discharge cycling was conducted on a LAND-2010 automatic battery tester in the voltage window of 1.0-3.0 V. Cyclic voltammetry (CV), electrochemical impedance spectroscopy (EIS) and galvanostatic intermittent titration technique (GITT) were performed on a Bio-Logic VSP multichannel potentiostatic-galvanostatic system. The impedance data were recorded by applying an *ac* voltage of 5 mV in the frequency range from 1 MHz to 5 mHz. GITT measurement was performed throughout the first discharge process. For each GITT step, the battery was discharged with a current flux of 30 mA g^{-1} for 0.5 h, followed by an open circuit stand for 4 h to reach the quasi-equilibrium state.

3. Results and discussion

3.1 X-ray diffraction

As the first step for materials preparation, the TiN nano particles were heat treated at 400 ^oC in air to obtain the precursors. X-ray diffraction shows that the precursor is a mixture of anatase, rutile and TiN due to incomplete reaction of TiN with oxygen (Supporting Information, Figure S1). The amount of N in the precursors could be adjusted by changing the heat treatment time. In order to prepare pure TiO_2-B nanowires, the heat treatment temperature should be increased to 500 ^oC and the heating time should be elongated to 10 h. Thereafter, the final products could be obtained by the hydrothermal reaction of the precursors. Totally, five samples were prepared in this work and their crystal structures were examined by XRD. Figure 1 shows the XRD patterns of the pure TiO_2-B and two typical N-doped TiO_2-B

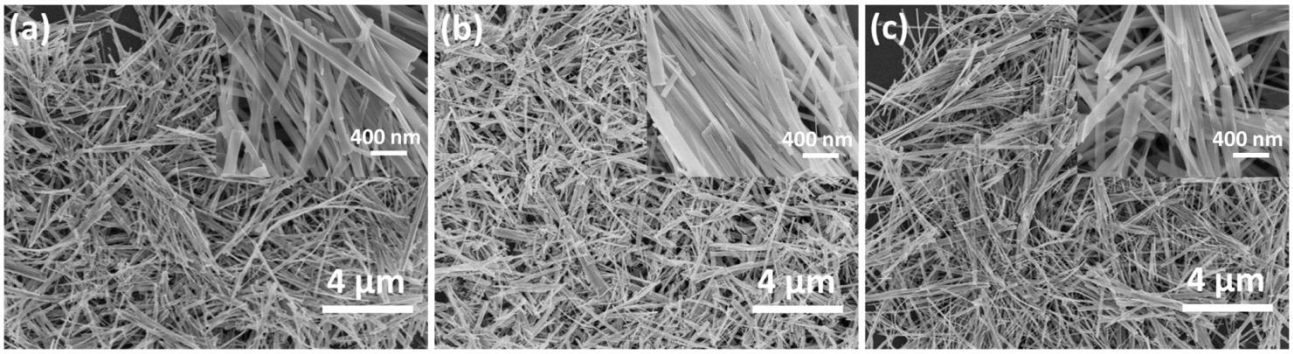

Figure 2. SEM images of the P-TiO_2 (a), I-TiO_2 (b) and I/S-TiO_2 (c) samples.

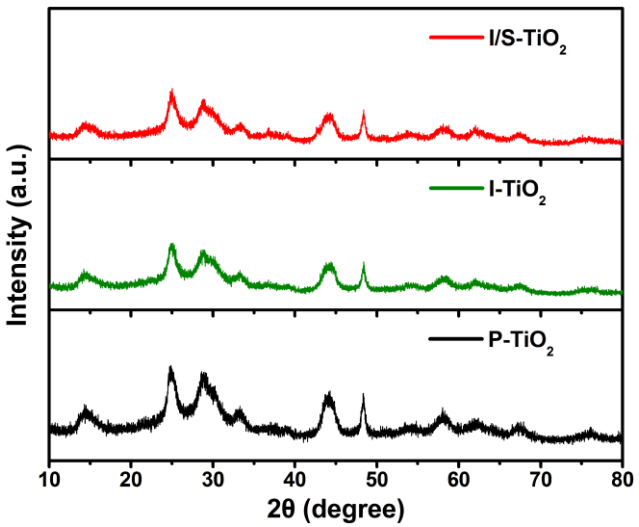

Figure 1. XRD patterns of the P-TiO_2, I-TiO_2 and I/S-TiO_2 samples.

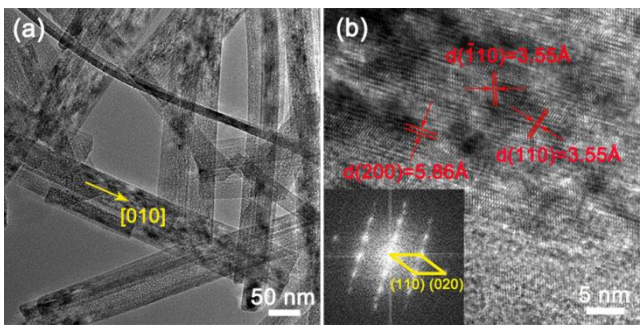

Figure 3. (a) TEM and (b) HRTEM images of the pure TiO_2-B nanowires. Inset in (b) shows the fast Fourier transform of the HRTEM image.

samples. All patterns exhibit the elaborate diffraction peaks of TiO_2-B that having a monoclinic structure with space group *C*2/*m*. The diffraction peaks are broad indicating that the products are nano sized materials. The framework of TiO_2-B is constructed by corrugated sheets of edge- and corner-sharing TiO_6 octahedra that are linked by bridging oxygen atoms to form a three-dimensional network.[35] This structure is more open than those of rutile and anatase TiO_2, making the material a more effective host for lithium storage. The lattice parameters of the pure TiO_2-B nanowires are calculated to be a = 12.288 Å, b = 3.759 Å, c = 6.482 Å, β = 107.06º, and V = 286.23 $Å^3$ which fit well with those recorded in JCPDS 74-1940. The lattice parameters of the N-doped TiO_2-B samples are similar as those of pure TiO_2-B. The diffraction peaks of these nano materials are weak and broad. In addition, the N doping contents are small and the size of N^{3-} (r = 1.46 Å) is similar to that of O^{2-} (r = 1.36 Å). Due to these reasons, it is difficult to discern the slight changes of the N-doped TiO_2-B materials from the present XRD patterns.

3.2 Morphology and microstructure characterizations

The morphologies of the pure and N-doped TiO_2-B samples are studied by SEM as shown in Figure 2. All the samples are composed of nanowires showing a high aspect ratio with 50-200 nm in width and several micrometers in length. Owing to the freeze-drying treatments, the samples show good dispersion without significant agglomeration and twine. These features are conducive to electrode materials in touch with electrolyte more effectively thus resulting in satisfying battery performance. The pure TiO_2-B is further studied by TEM as shown in Figure 3. In the HRTEM image, the lattice fringes with spaces of 0.586 nm and 0.355 nm are due to the (200) and (110) planes of TiO_2-B, respectively. In addition, fast Fourier transform(FFT) of the HRTEM image shows that the TiO_2-B nanowire grows along the [010] direction. The N-doped TiO_2-B samples show similar TEM and HRTEM images as those of pristine TiO_2-B indicating that N doping does not change the atomic structure of TiO_2-B. In order

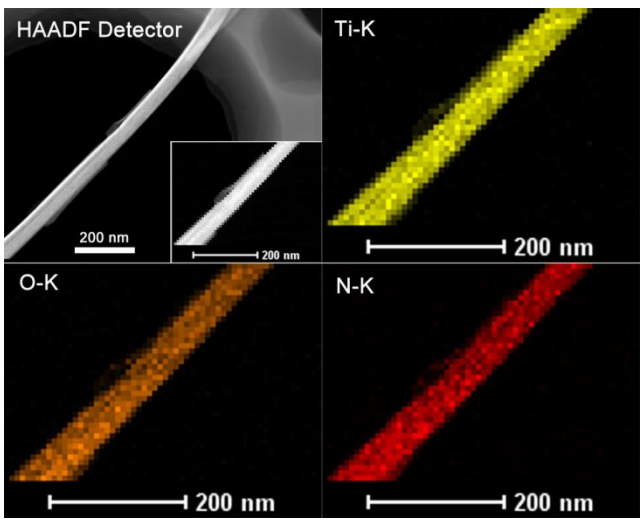

Figure 4. HAADF-STEM image and mapping of the Ti, O and N elements of the I/S-TiO_2 sample. The elemental map signals were obtained by scanning the inset of the HAADF-STEM image.

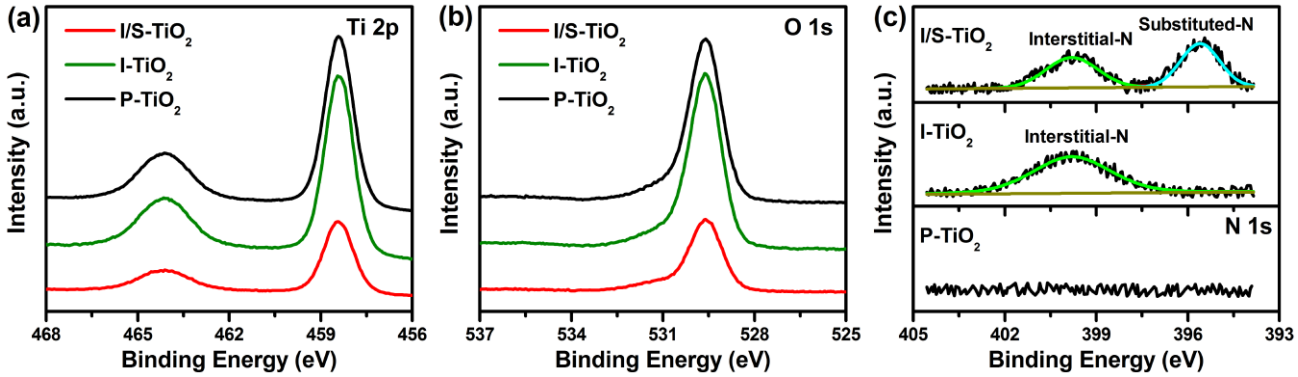

Figure 5. Ti 2p (a), O 1s (b), and N 1s (c) XPS of the P-TiO_2, I-TiO_2 and I/S-TiO_2 samples.

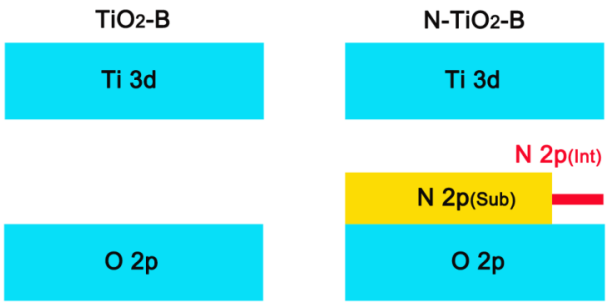

Figure 6. Scheme of the band structures of the pure and N-doped TiO_2-B.

Table 1. Electronic conductivity of the P-TiO_2, I-TiO_2 and I/S-TiO_2 samples.

	P-TiO_2	I-TiO_2	I/S-TiO_2
Electronic Conductivity [S cm^{-1}]	3.01×10^{-11}	3.81×10^{-9}	4.61×10^{-8}

to confirm doping of N in the TiO_2-B nanowires, we carried out EDX analysis for a single nanowire. Figure 4 shows the dispersive mapping of the Ti, O, N elements which indicates that the N element is uniformly distributed in the material.

3.3 X-ray photoelectron spectroscopy

XPS analysis was performed to study the chemical states of Ti, O and N of the materials. All samples show very similar Ti 2p and O 1s XPS as shown in Figure 5a and 5b, respectively. The Ti $2p_{3/2}$ binding energy is observed at 458.4 eV which fits well with that of Ti^{4+}.[36] The O 1s binding energy at 529.6 eV confirms the O^{2-} state of the materials.[36] As shown in Figure 5c, no N 1s XPS is observed for the pure TiO_2-B nanowires, but the appearance of N 1s XPS for the N-doped TiO_2-B samples confirm the successful doping of N in TiO_2-B. The N 1s peak at 399.8 eV is due to the interstitial-N with the O-Ti-N linkage, and the other one at 395.6 eV is due to the substituted-N with the direct Ti-N linkage.[37] The interstitial O-Ti-N bond shows a higher binding energy than that of the substituted Ti-N because the high electro-negativity of oxygen reduces the electron density on nitrogen. The amounts of interstitial/substituted-N in the samples are calculated to be 0.57/0.72 at.%, 0.52/0 at.%, respectively. According to the N 1s XPS results of all the prepared samples (Supporting Information, Figurer S2), it can be concluded that the N dopants preferentially occupy the interstitial site of TiO_2-B up to a content of ~ 0.55 at.%. Above this critical value, the N dopants will substitute the oxygen atoms of TiO_2-B. In addition, the maximum substituted-N in the samples is evaluated to be ~ 1.3 at.%; otherwise, TiN impurity will be formed in the material. It has reported that the substituted-N is more effective than the interstitial-N for improving the electronic conductivity of TiO_2 because it could narrow the band gap of TiO_2 by elevating the valence band maximum, while the interstitial-N can only introduce some localized N 2p states in the band gap, as shown in Figure 6.[30] Accordingly, the interstitial/substituted-N co-doped TiO_2-B (hereafter denoted as I/S-TiO_2) is expected to possess a higher electronic conductivity than those of the interstitial-N doped TiO_2-B (hereafter denoted as I-TiO_2) and pure TiO_2-B (hereafter denoted as P-TiO_2). As shown in Table 1, dc conductivity measurement shows that the electronic conductivity of the pure TiO_2-B nanowires is 3.01×10^{-11} S cm^{-1}. The I-TiO_2 sample which contains only interstitial-N shows a larger electronic conductivity of 3.81×10^{-9} S cm^{-1}. Significantly, the I/S-TiO_2 sample containing both interstitial and substituted-N possesses the largest electronic conductivity of 4.61×10^{-8} S cm^{-1}.

3.4 Raman scattering

As above mentioned, the substituted-N is very important for improving the electronic conductivity of TiO_2-B. In order to know the possible substitute positions of N, we carried out Raman scattering to study the local structure of the samples. The Ti atoms in TiO_2-B has different local environments, namely Ti(1) and Ti(2). Both of them are surrounded by six oxygen atoms as shown in the inset of Figure 7. Group theory calculations have shown 18 Raman active modes for TiO_2-B most of which can be observed in Figure 7.[38] In general, the Raman patterns of the three samples are similar except two major differences. First, the peak intensities of P-TiO_2 and I-TiO_2 are much stronger than those of I/S-TiO_2. Even though multiple factors can affect the intensities of Raman peaks, here we can rule out the effects of measurement conditions because all the experiments were performed at the same conditions (including sample amount, laser power, scattering time et al). Therefore, the differences in Raman intensities could be attributed to the intrinsic properties of the samples. One of the possible reasons may be due to the higher electronic conductivity of I/S-TiO_2. It is

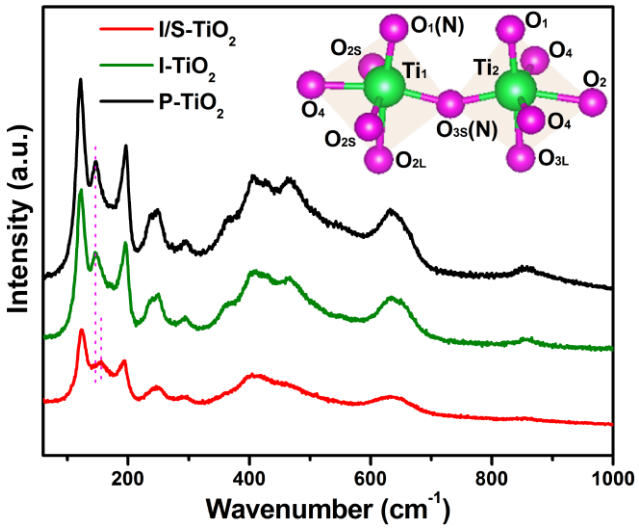

Figure 7. Raman spectrum of the P-TiO_2, I-TiO_2 and I/S-TiO_2 samples. (Inset): scheme of the local structure of TiO_2-B.

known that the material with a high electronic conductivity could reduce the skin depth of the incident photons, thus resulting in low Raman scattering intensities. Second, the positions of all peaks are very stable only the one located at around 145.6 cm^{-1} (dash line) for exception. This Raman peak is attributed to the Ti(1)-O_1-Ti(2) and O_1-Ti(1)- O_3 vibrations ofTiO_2-B.[38] For the I-TiO_2 sample, this Raman peak still locates at 145.6 cm^{-1} which is the same as that of P-TiO_2. This indicates that the interstitial-N has little impact on the local structure of TiO_2-B. However, for I/S-TiO_2 that having both interstitial and substituted-N, this peak shifts to a higher wavenumber of 154.3 cm^{-1}. This indicates that the substituted-N replaces the O atoms at the O_1 and/or O_3 positions. In addition, the local structures related with the Ti(1)-O_1-Ti(2) and O_1-Ti(1)-O_3 bonds are strengthened by the substituted-N atoms.

3.5 Galvanostatic charge-discharge cycling

Figure 8a compares the first charge-discharge curves of the samples at the 0.5 C rate (1C = 300 mA g^{-1}). All the samples display a pair of S-shaped voltage profiles, which are different from the characteristic voltage plateaus at ~ 1.7 V for anatase TiO_2. This is due to the different Li ion intercalation mechanisms of TiO_2-B and anatase. It has reported that the Li^+ intercalation into TiO_2-B is a pseudo-capacitive process, rather different from the two-phase diffusion process of anatase.[39, 40] This makes TiO_2-B very attractive for fast Li ion transport. The initial discharge/charge capacities for the pure TiO_2-B nanowires are 240.9/217.4 mAh g^{-1} resulting in a columbic efficiency of 90.2 %. The initial capacity loss could be due to Li ion storage at irreversible sites. Also, a part of the capacity loss could be caused by formation of solid electrolyte interface (SEI) film as recently reported by P. G. Bruce et al.[41] The initial discharge/charge capacities of the samples increase with N-doping. Especially, I/S-TiO_2 (277.8/249.0 mAh g^{-1}) shows larger specific capacities than those of I-TiO_2 (252.0/225.5 mAh g^{-1}).

Figure 8b shows the rate performance of the pure and N-doped TiO_2-B samples. The corresponding charge-discharge curves at each current rate are displayed in Figure 8d to 8f. At each charge-discharge rate, I-TiO_2 only shows slightly higher capacities than those of P-TiO_2. In contrast, the discharge capacities of I/S-TiO_2 are much higher than those of I-TiO_2 and P-TiO_2. When the charge-discharge rate increases to 100 C (30 A g^{-1}), I/S-TiO_2 still has a high discharge capacity of 100 mAh g^{-1}, whereas that of P-TiO_2 is only 75 mAh g^{-1}. In addition, comparing to the big fluctuations of pure TiO_2-B, the specific capacities of I/S-TiO_2 are very stable at this extremely high charge-discharge rate. Further, the normalized discharge capacities (Supporting Information, Figure S3) also shows that the rate capability of the N-doped samples, especially I/S- TiO_2, are better than that of P-TiO_2 especially at high current rates. The cycle stability is also important for the practical applications of lithium-ion batteries.

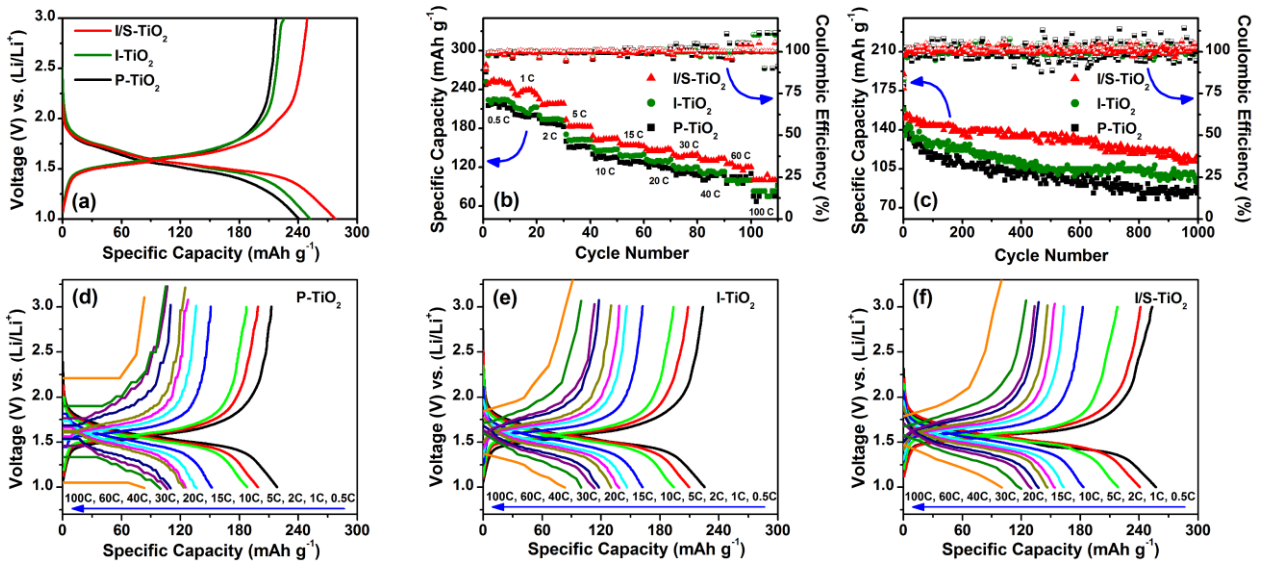

Figure 8. (a) The first charge-discharge curves, (b) rate-dependent cycling performance, and (c) long term cycling stability of the samples. (d-f) charge-discharge curves of the samples at different current rates.

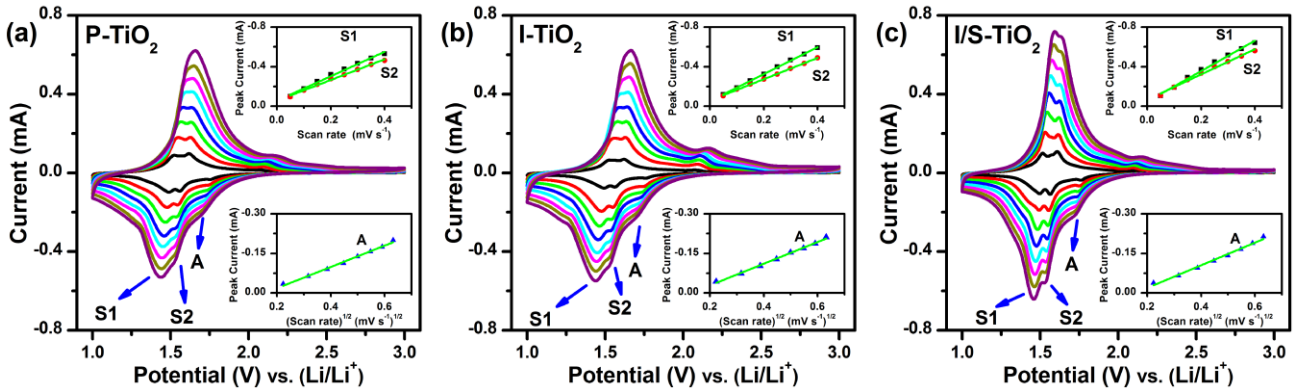

Figure 9. CV curves of the P-TiO_2 (a), I-TiO_2 (b) and I/S-TiO_2 (c) samples at different scan rates. (Inset): linear fitting of the cathodic current vs. scan rate.

Here the long term cycling stability of the pure and N-doped TiO_2-B samples are tested at the 20 C rate as shown in Figure 8c. The pure TiO_2-B nanowires exhibits fast capacity fading in the initial 100 cycles. Then the discharge capacity gradually decreases which is only 85 mAh g^{-1} after 1000 cycles. The corresponding capacity retention is 60 %. I-TiO_2 shows slightly improved cycling performance but the capacity retention is still unsatisfying. More excitingly, I/S-TiO_2 shows much better capacity retention. A high discharge capacity of 116 mAh g^{-1} can be obtained after 1000 cycles, and the capacity retention increases to 76 %. This indicates that the substituted-N is much more effective than the interstitial-N for improving the electrochemical performance of TiO_2-B. We also studied the long term cycling performance (Supporting Information, Figure S4) and rate performance (Supporting Information, Figure S5) of all the prepared samples. Overall, the interstitial/substituted-N co-doped samples show much better rate capability and cycle stability than those of the other samples. This further demonstrates that the substituted-N is very important for improving the electrochemical properties of TiO_2-B.

3.6 Cyclic voltammetry

Figure 9 shows the CV curves of the pure and N-doped TiO_2-B nanowires at different scan rates. The peak-S1 and -S2 are due to Li extraction from the TiO_2-B phase. At present there are two different point-of-views regarding the origin of peak-A. Some people think that this peak is due to an anatase impurity phase because TiO_2-B is metastable so that a part of the material could be transformed to anatase during heat treatment process.[42-44] On the other hand, recent theoretical and experimental studies have shown that the peak-A is attributed to Li^+ intercalation into the interstitial octahedral site of TiO_2-B.[45, 46] Even though there is not a definite conclusion up to now, this peak is always observed for TiO_2-B samples. At the scan rate of 0.1 mV s^{-1}, the electrode polarizations (i.e. the voltage splitting between the anodic and cathodic peaks) for the pure TiO_2-B nanowires are 0.08 V for peak-S1 and 0.09 V for peak-S2 which are smaller than that of 0.36 V for peak-A. This indicates that the electrochemical kinetics during the peak-S1 and -S2 processes are better than that during peak-A. The corresponding electrode polarizations for I/S-TiO_2 (i.e., 0.04 V, 0.06 V, 0.34 V) and I-TiO_2 (i.e., 0.07 V, 0.08 V, 0.35 V) are smaller than those of P-TiO_2 indicating that N-doping improves the electrochemical kinetics of the electrode.

CV analysis was further used to study the Li ion storage mechanisms of the pristine and N-doped TiO_2-B samples. For all the three samples, the peak-S1 and -S2 display linear relationships against the scan rate (inset of Figure 9), which is characteristic for the capacitive behaviour:[8]

$$I_p = dQ/dt = CdE/dt = Cv \qquad (1)$$

where Q is the voltammetric charge, C is capacitance and dE/dt is the scan rate (v). The small peak-to-peak splitting (i.e. electrode polarization) is a typical feature of faradaic pseudo-capacitance which is different from the ideally rectangle CV curves of double-layer capacitance. On the other hand, the peak-A shows a linear relationship against the square root of scan rate ($v^{1/2}$) which is corresponding to a typical feature of the diffusion-controlled process:[47, 48]

$$I_p = 2.69\times10^5 A\cdot C\cdot D_{Li}^{1/2}\cdot n^{3/2}\cdot v^{1/2} \qquad (2)$$

where I_p is the peak current, A is the electrode surface area, C is the concentration of Li ions in the electrode, n is the number of electrons involved in the redox process, v is the scan rate. The specific faradaic pseudo-capacitance behaviour of TiO_2-B is much favourable for fast Li ion intercalation and de-intercalation thus resulting in its excellent rate capability. Table 2 shows the slopes of the fitted lines. For each current peak, the N-doped samples always show a larger slope than that of pure TiO_2-B nanowires. Especially, I/S-TiO_2 possesses the largest slopes in all the three samples. This indicates that the substituted-N is more effective than the interstitial-N for improving the electrochemical kinetics of TiO_2-B.

Table 2. Slopes of the fitted lines for the S1, S2 and A current peaks

	S1[a]	S2[a]	A[b]
I/S-TiO_2	-1.54	-1.27	-0.43
I-TiO_2	-1.36	-1.08	-0.41
P-TiO_2	-1.24	-1.05	-0.40

[a]Linear fitting of the cathodic current versus (scan rate).

[b] Linear fitting of the cathodic current versus (scan rate)$^{1/2}$.

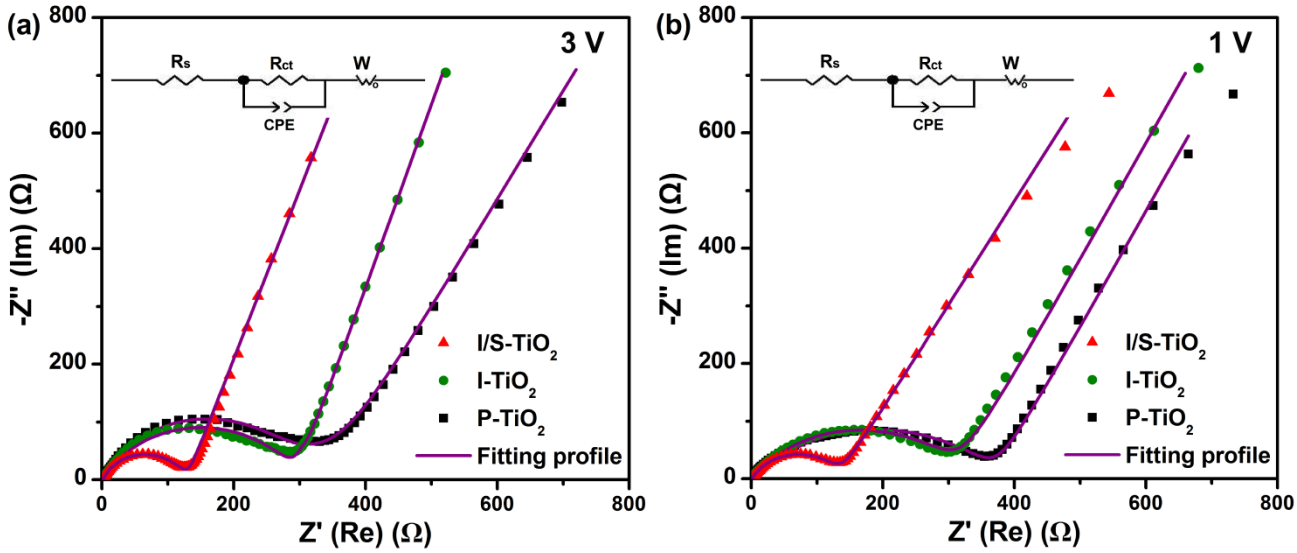

Figure 10. Nyquist plots of the P-TiO_2, I-TiO_2 and I/S-TiO_2 samples at 3.0 V (a) and 1.0 V (b) of the first discharge. (Inset): equivalent circuit of the Nyquist plots.

Table 3. The fitted electrochemical kinetic parameters of the P-TiO_2, I-TiO_2 and I/S-TiO_2 samples

	R_s (Ω)		R_{ct} (Ω)		D_{Li} ($cm^2\ s^{-1}$)	
	3.0 V	1.0 V	3.0 V	1.0 V	3.0 V	1.0 V
I/S-TiO_2	1.3	1.1	129.2	135.0	1.06×10^{-8}	1.14×10^{-9}
I-TiO_2	1.4	1.2	286.7	320.9	9.58×10^{-9}	8.14×10^{-10}
P-TiO_2	1.8	1.7	327.1	376.1	4.50×10^{-9}	7.34×10^{-10}

3.7 Electrochemical impedance spectroscopy

The electrochemical process of lithium ion batteries involves charge transfer reactions at the electrode/electrolyte interface and Li ion diffusion in the electrode bulk. In order to study the electrochemical kinetics of the materials, *ac* impedance spectroscopy was collected at 3.0 V and 1.0 V of the first discharge. Figure 10 shows the Nyquist plots of the pristine and N-doped TiO_2-B materials. All samples show a semicircle in the high to medium frequency region which is attributed to the charge transfer process. The Nyquist plots are simulated by the equivalent circuit shown in the inset of Figure 10 where R_s represents the ohmic resistance of the battery cell, R_{ct} and *CPE* represent the charge transfer resistance and the correlated constant phase element, while *W* is related to the diffusion of Li ions in the active materials. The fitted kinetic parameters are displayed in Table 3. All samples show very small ohmic resistances (< 2.0 Ω). The N-doped TiO_2-B, especially I/S-TiO_2, show smaller ohmic resistances than that of P-TiO_2 which could be attributed to their high electronic conductivities assuming all battery cells were assembled in the same way. For each sample, the charge transfer resistance slightly increases with the cell discharged from 3.0 V to 1.0 V. The N-doped TiO_2 samples show smaller charge transfer resistances than the pristine one. Especially, the charge transfer resistances of I/S-TiO_2 are much smaller than those of P-TiO_2 and I-TiO_2. This indicates that the substituted-N significantly improves the charge transfer reactivity of TiO_2-B.

The Warburg data of Nyquist plots was used to determine the lithium diffusion coefficients (D_{Li}) of the materials by using the following equation,[49]

$$D_{Li} = \frac{1}{2}\left[\left(\frac{V_M}{FS\sigma}\right)\left(\frac{dE}{dx}\right)\right]^2 \quad (3)$$

where V_m is the molar volume of TiO_2-B, *S* is the surface area of the electrode, *F* is the Faraday constant, *dE/dx* is the first order derivative of the discharge profile. σ is the Warburg coefficient which obeys the following relationship,

$$\sigma = \frac{dZ'}{d\omega^{-1/2}} \quad (4)$$

σ can be obtained from the slope of the linear fitting of Z' *vs.* $\omega^{-1/2}$ plots (Supporting Information, Figure S6). Based on this, the lithium diffusion coefficients of the samples are calculated and displayed in Table 3. It is seen that the lithium diffusion coefficients are improved by N-doping, especially by the substituted-N. In addition, the lithium diffusion coefficient decreases about one order of magnitude with the cell discharged from 3.0 V to 1.0 V. Detailed discussion of the lithium diffusion kinetic properties will be given in the following section according to the GITT analysis results.

3.8 Galvanostatic intermittent titration technique

GITT has been widely used to determine the lithium diffusion coefficients (D_{Li}) of electrode materials with highly reliable data. Figure 11 shows the GITT curves of the samples during the first discharge as a function of Li^+ content (*x*). The plots of *dE/dx vs. x* are presented in the inset of Figure 11. Considering that the Li^+ intercalation in TiO_2-B obeys a solid solution behaviour, the lithium diffusion coefficients can be calculated by the following equation,[50, 51]

$$D_{Li} = \frac{4}{\pi}\left(I_0 \frac{V_M}{FS}\right)^2 \left(\frac{dE/dx}{dE/dt^{1/2}}\right)^2 \quad (5)$$

where I_0 is the applied current, V_m is the molar volume of the active material, F is the Faraday constant and S is the surface area of the electrode. Figure S7 (Supporting Information) shows a typical titration step of the samples at x = 0.49. It is seen that I/S-TiO_2 and I-TiO_2 show smaller ohmic polarizations and overpotentials than those of P-TiO_2 due to their high electronic conductivities. Figure S8 (Supporting Information) shows the E *vs.* $t^{1/2}$ plots of the materials at x = 0.49 where a linear relationship can be obtained in the time range of 10 ~ 100 *s*. Thus, the lithium diffusion coefficient can be calculated by Equ. (5) using the values of dE/dx and $dE/dt^{1/2}$. Figure 12 shows the lithium diffusion coefficients of the samples as a function of Li^+ content. It is noticed that the GITT results at 3.0 V and 1.0 V are about one order of magnitude lower than those obtained by the EIS analysis. The discrepancy between GITT and EIS results has been clarified by Bruce et al.[52] and some other groups.[50, 53] According to these literatures, GITT could provide more precise lithium diffusion coefficients as compared to EIS. All samples show similar D_{Li} of ~ 10^{-9} cm^2 s^{-1} in the x range of $0 < x < 0.68$. The D_{Li} of P-TiO_2 gradually decreases with further Li^+ intercalation and reaches to a minimum value of 2.69 × 10^{-11} cm^2 s^{-1} at x = 0.82. Afterwards, the D_{Li} values are almost unchanged until a maximum Li^+ content of ~ 0.92 is obtained. According to K. Hoshina et al. the small D_{Li} for $x > 0.68$ could be attributed to distortion of the Li^+ diffusion channel along the *b*-axis of TiO_2-B.[54] This diffusion channel is constructed by the Ti(1) and Ti(2) atoms and the linkage O_1 and O_3 oxygens (Figure 13). Raman scattering shows that the substituted-N in I/S-TiO_2 strengthens the Ti(1)-O_1-Ti(2) and O_1-Ti(1)-O_3 bonds. This will improve the stability of the corresponding local structures thus depresses the distortion of the Li^+ diffusion channel. Therefore, the material can possess large D_{Li} in a wilder x range thus resulting in a larger discharge capacity. As can be seen from Figure 12, the D_{Li} of I/S-TiO_2 could be kept at ~ 10^{-9} cm^2 s^{-1} until x = 0.83. In addition, the maximum Li^+ intercalation amount increases to 1.07 which is much larger than that of P-TiO_2. In fact, the interstitial-N also improves the lithium diffusion to some extent. But it plays less important effect on the diffusion kinetics of TiO_2-B than the substituted-N does. As seen from Figure 12, the D_{Li} of I-TiO_2 begin to decrease at x = 0.73. In addition, even though the total Li^+ intercalation of I-TiO_2 (~ 0.97) is larger than that of P-TiO_2, it is still much less than that of I/S-TiO_2. Therefore, the substituted-N is much more effective than the interstitial-N for improving the electrochemical performance of TiO_2-B.

4. Conclusions

In summary, N-doped TiO_2-B nanowires have been prepared by the solvothermal method using TiN nano particles as the starting material. The N dopants preferentially occupy the interstitial sites of TiO_2-B. The maximum amount of interstitial-N is about 0.55 at.%. Above this critical value, the N dopants will substitute the oxygen atoms at the O_1 and/or O_3 positions. The maximum substituted-N in TiO_2-B is ~ 1.3 at.%; otherwise, TiN impurity will be formed in the material. The interstitial-N has little impact on the structure and physical properties of TiO_2-B. In contrast, the substituted-N is very important for improving the electronic conductivity and local structural stability of TiO_2-B. This significantly improves the electrochemical properties of the TiO_2-

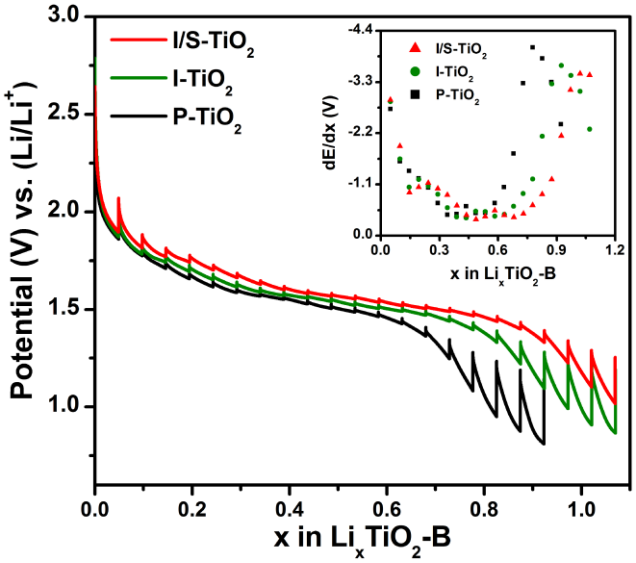

Figure 11. GITT curves of the P-TiO_2, I-TiO_2 and I/S-TiO_2 samples. (Inset): dE/dx values of the GITT curves.

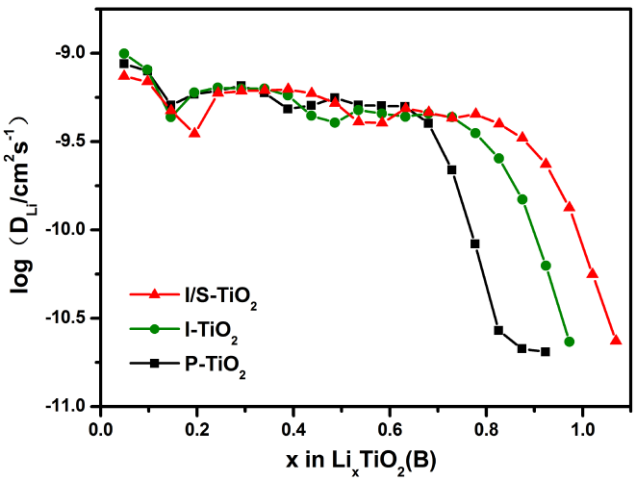

Figure 12. D_{Li} values of the P-TiO_2, I-TiO_2 and I/S-TiO_2 samples as a function of Li^+ content.

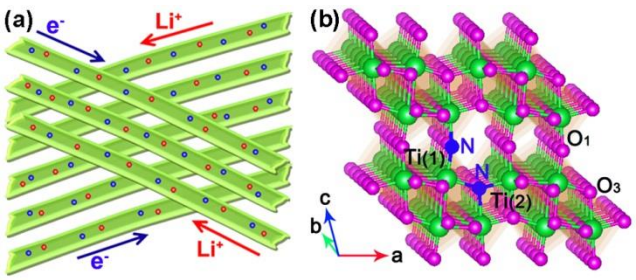

Figure 13. (a) Li^+/e^- transport pathway for the TiO_2-B nano wires. (b) Scheme of the lattice structure for N-doped TiO_2-B.

B nanowires. As a result, the practical specific capacities, rate capability and cycle stability of the material are overall improved by the substituted-N dopants. The material shows a discharge capacity of 153 mAh g^{-1} at the 20 C rate with a capacity retention ability of 76 % after 1000 cycles. In addition, it can deliver a discharge capacity of 100 mAh g^{-1} at an ultra-high rate of 100 C (I = 30 A g^{-1}), indicating its great potential in high power lithium ion batteries.

Acknowledgements

This work was supported by the 973 Program (No. 2015CB251103), National Natural Science Foundation of China (No. 51472104, 21473075, 51272088), and the National Found for Fostering Talents of Basic Science (No. J1103202).

Notes and references

1. G. N. Zhu, Y. G. Wang and Y. Y. Xia, *Energy & Environmental Science*, 2012, **5**, 6652-6667.
2. Z. Chen, I. Belharouak, Y. K. Sun and K. Amine, *Advanced Functional Materials*, 2013, **23**, 959-969.
3. X. Yan, Y. J. Li, F. Du, K. Zhu, Y. Q. Zhang, A. Y. Su, G. Chen and Y. J. Wei, *Nanoscale*, 2014, **6**, 4108-4116.
4. V. Gentili, S. Brutti, L. J. Hardwick, A. R. Armstrong, S. Panero and P. G. Bruce, *Chemistry of Materials*, 2012, **24**, 4468-4476.
5. J. Wang, J. Polleux, J. Lim and B. Dunn, *Journal of Physical Chemistry C*, 2007, **111**, 14925-14931.
6. Y. S. Hu, L. Kienle, Y. G. Guo and J. Maier, *Advanced Materials*, 2006, **18**, 1421-1426.
7. J. Kong, Y. Wei, C. Zhao, M. Y. Toh, W. A. Yee, D. Zhou, S. L. Phua, Y. Dong and X. L. Lu, *Nanoscale*, 2014, **6**, 4352-4360.
8. M. Zukalova, M. Kalbac, L. Kavan, I. Exnar and M. Graetzel, *Chemistry of Materials*, 2005, **17**, 1248-1255.
9. Y. Yang, H. Wang, Q. Zhou, M. Kong, H. Ye and G. Yang, *Nanoscale*, 2013, **5**, 10267-10274.
10. Z. Hong, M. Wei, T. Lan and G. Cao, *Nano Energy*, 2012, **1**, 466-471.
11. G. Armstrong, A. R. Armstrong, P. G. Bruce, P. Reale and B. Scrosati, *Advanced Materials*, 2006, **18**, 2597-2600.
12. S. H. Kang, V. G. Pol, I. Belharouak and M. M. Thackeray, *Journal of the Electrochemical Society*, 2010, **157**, A267-A271.
13. N. Arun, V. Aravindan, S. Jayaraman, N. Shubha, W. C. Ling, S. Ramakrishna and S. Madhavi, *Nanoscale*, 2014, **6**, 8926-8934.
14. A. R. Armstrong, G. Armstrong, J. Canales and P. G. Bruce, *Angewandte Chemie-International Edition*, 2004, **43**, 2286-2288.
15. J. Qu, Q. D. Wu, Y. R. Ren, Z. Su, C. Lai and J. N. Ding, *Chemistry-an Asian Journal*, 2012, **7**, 2516-2518.
16. C. Chen, X. Hu, P. Hu, Y. Qiao, L. Qie and Y. Huang, *European Journal of Inorganic Chemistry*, 2013, **2013**, 5320-5328.
17. C. Chen, X. Hu, Z. Wang, X. Xiong, P. Hu, Y. Liu and Y. Huang, *Carbon*, 2014, **69**, 302-310.
18. Y. Furuya, W. Zhao, M. Unno and H. Noguchi, *Electrochimica Acta*, 2014, **136**, 266-273.
19. S. Liu, Z. Wang, C. Yu, H. B. Wu, G. Wang, Q. Dong, J. Qiu, A. Eychmueller and X. W. Lou, *Advanced Materials*, 2013, **25**, 3462-3467.
20. H. Huang, J. Fang, Y. Xia, X. Tao, Y. Gan, J. Du, W. Zhu and W. Zhang, *Journal of Materials Chemistry A*, 2013, **1**, 2495-2500.
21. M. Zhen, S. Guo, G. Gao, Z. Zhou and L. Liu, *Chemical communications (Cambridge, England)*, 2014, **51**, 507-510.
22. M. Srivastava, J. Singh, T. Kuila, R. K. Layek, N. H. Kim and J. H. Lee, *Nanoscale*, 2015, **7**, 4820-4868.
23. T. Nikolay, L. Larina, O. Shevaleevskiy and B. T. Ahn, *Energy & Environmental Science*, 2011, **4**, 1480-1486.
24. Y. Wang, B. M. Smarsly and I. Djerdj, *Chemistry of Materials*, 2010, **22**, 6624-6631.
25. A. Ly Tuan, A. K. Rai, T. Trang Vu, J. Gim, S. Kim, E. C. Shin, J. S. Lee and J. Kim, *Journal of Power Sources*, 2013, **243**, 891-898.
26. R. Asapu, V. M. Palla, B. Wang, Z. Guo, R. Sadu and D. H. Chen, *Journal of Photochemistry and Photobiology a-Chemistry*, 2011, **225**, 81-87.
27. S. K. Das, M. Gnanavel, M. U. M. Patel, C. Shivakumara and A. J. Bhattacharyya, *Journal of the Electrochemical Society*, 2011, **158**, A1290-A1297.
28. Z. Ali, S. N. Cha, J. I. Sohn, I. Shakir, C. Yan, J. M. Kim and D. J. Kang, *Journal of Materials Chemistry*, 2012, **22**, 17625-17629.
29. H. Han, T. Song, J. Y. Bae, L. F. Nazar, H. Kim and U. Paik, *Energy & Environmental Science*, 2011, **4**, 4532-4536.
30. W. Jiao, N. Li, L. Wang, L. Wen, F. Li, G. Liu and H. M. Cheng, *Chemical Communications*, 2013, **49**, 3461-3463.
31. H. G. Jung, C. S. Yoon, J. Prakash and Y. K. Sun, *Journal of Physical Chemistry C*, 2009, **113**, 21258-21263.
32. J. G. Kim, D. Shi, K. J. Kong, Y. U. Heo, J. H. Kim, M. R. Jo, Y. C. Lee, Y. M. Kang and S. X. Dou, *ACS Applied Materials & Interfaces*, 2013, **5**, 691-696.
33. Y. Li, Z. Wang and X. Lv, *Journal of Materials Chemistry A*, 2014, **2**, 15473-15479.
34. Y. Q. Zhang, F. Du, X. Yan, Y. M. Jin, K. Zhu, X. Wang, H. M. Li, G. Chen, C. Z. Wang and Y. J. Wei, *ACS Applied Materials & Interfaces*, 2014, **6**, 4458-4465.
35. D. Panduwinata and J. D. Gale, *Journal of Materials Chemistry*, 2009, **19**, 3931-3940.
36. Y. P. Yu, X. J. Xing, L. M. Xu, S. X. Wu and S. W. Li, *Journal of Applied Physics*, 2009, **105**, 123535.
37. J. Wang, D. N. Tafen, J. P. Lewis, Z. Hong, A. Manivannan, M. Zhi, M. Li and N. Wu, *Journal of the American Chemical Society*, 2009, **131**, 12290-12297.
38. M. Ben Yahia, F. Lemoigno, T. Beuvier, J. S. Filhol, M. Richard Plouet, L. Brohan and M. L. Doublet, *Journal of Chemical Physics*, 2009, **130**, 204501.
39. A. G. Dylla, G. Henkelman and K. J. Stevenson, *Accounts of Chemical Research*, 2013, **46**, 1104-1112.
40. L. Kavan, M. Kalbac, M. Zukalova, I. Exnar, V. Lorenzen, R. Nesper and M. Graetzel, *Chemistry of Materials*, 2004, **16**, 477-485.
41. S. Brutti, V. Gentili, H. Menard, B. Scrosati and P. G. Bruce, *Advanced Energy Materials*, 2012, **2**, 322-327.
42. H. Liu, Z. Bi, X. G. Sun, R. R. Unocic, M. P. Paranthaman, S. Dai and G. M. Brown, *Advanced Materials*, 2011, **23**, 3450-3454.
43. Z. Sun, X. Huang, M. Muhler, W. Schuhmann and E. Ventosa, *Chemical Communications*, 2014, **50**, 5506-5509.
44. J. Prochazka, L. Kavan, M. Zukalova, O. Frank, M. Kalbac, A. Zukal, M. Klementova, D. Carbone and M. Graetzel, *Chemistry of Materials*, 2009, **21**, 1457-1464.
45. S. T. Myung, N. Takahashi, S. Komaba, C. S. Yoon, Y.-K. Sun, K. Amine and H. Yashiro, *Advanced Functional Materials*, 2011, **21**, 3231-3241.
46. A. R. Armstrong, C. Arrouvel, V. Gentili, S. C. Parker, M. S. Islam and P. G. Bruce, *Chemistry of Materials*, 2010, **22**, 6426-6432.
47. H. Lindström, S. Södergren, A. Solbrand, H. Rensmo, J. Hjelm, A. Hagfeldt and S. E. Lindquist, *Journal of Physical Chemistry B*, 1997, **101**, 7717-7722.
48. T. Jiang, W. Pan, J. Wang, X. Bie, F. Du, Y. Wei, C. Wang and G. Chen, *Electrochimica Acta*, 2010, **55**, 3864-3869.
49. C. Ho, I. D. Raistrick and R. A. Huggins, *Journal of The Electrochemical Society*, 1980, **127**, 343-350.
50. S. Yang, X. Wang, X. Yang, Y. Bai, Z. Liu, H. Shu and Q. Wei, *Electrochimica Acta*, 2012, **66**, 88-93.
51. W. Weppner and R. A. Huggins, *Journal of the Electrochemical Society*, 1977, **124**, 1569-1578.
52. P. G. Bruce (Ed.), *Solid-State Electrochemistry Cambridge University Press*, 1995, **ch. 7** (by W. R. McKinnon), p. 163; **ch. 8** (by W. Weppner), p. 199.
53. C. J. Wen, B. A. Boukamp and R. A. Huggins, *Journal of The Electrochemical Society*, 1979, **126**, 2258-2266.
54. K. Hoshina, Y. Harada, H. Inagaki and N. Takami, *Journal of the Electrochemical Society*, 2014, **161**, A348-A354.